Nonmetal Oxygen Vacancies for Catalysis under Cover

Qiuwen Liu[1], Qiang Liu[1], Yawei Wu[1], Fangshu Xing[1], Chuchu Cheng[1], and Caijin Huang[2]

[1]Affiliation not available
[2]State Key Laboratory of Photocatalysis on Energy and Environment

May 26, 2020

Abstract

In heterogeneous catalysis, oxygen vacancies of metal oxides play a key role by modulating properties of coordination, electron states, electrical conductivity, and surface property. However, the investigation of oxygen vacancies in nonmetal oxides and their catalytic applications have rarely been reported. Here, we present oxygen vacancies-rich BPO4 hollow spheres covered by few-layer hexagonal boron nitride (BN) with a sandwich-like structure (BN@BPO4@BN) through an in-situ growth method. The as-prepared catalyst showed better catalytic activity and higher selectivity than that of commercial BN in the oxidative dehydrogenation of propane to propene because of the synergetic effect between oxygen vacancies-rich BPO4 and h-BN. Oxygen vacancies increase the adsorption amount of propane and the confined space at the interface of BN and BPO4 weakens the adsorption of propene, benefiting the recycle of active sites. Moreover, the confined space and oxygen vacancies result in the transformation of reaction kinetic model.

In heterogeneous catalysis, oxygen vacancies of metal oxides play a key role by modulating properties of coordination, electron states, electrical conductivity, and surface property. However, the investigation of oxygen vacancies in nonmetal oxides and their catalytic applications have rarely been reported. Here, we present oxygen vacancies-rich BPO_4 hollow spheres covered by few-layer hexagonal boron nitride (BN) with a sandwich-like structure (BN@BPO_4@BN) through an in-situ growth method. The as-prepared catalyst showed better catalytic activity and higher selectivity than that of commercial BN in the oxidative dehydrogenation of propane to propene because of the synergetic effect between oxygen vacancies-rich BPO_4 and h-BN. Oxygen vacancies increase the adsorption amount of propane and the confined space at the interface of BN and BPO_4 weakens the adsorption of propene, benefiting the recycle of active sites. Moreover, the confined space and oxygen vacancies result in the transformation of reaction kinetic model.

Keywords: *nonmetal oxides, oxygen vacancies, catalysis under cover, sandwich-like hollow spheres, BN, BPO_4.*

Introduction

The surface state of the catalyst is a matter of great concern in heterogeneous catalysis, and plays a key role in improving catalytic activity and selectivity of reactions. Currently, the introduction of oxygen vacancy is one of the most popular strategies for modifying surface states. Oxygen vacancy is an anion defect with unsaturated coordination, and tends to generate localized electrons that can supply a portion of energy in reaction.[1] In the past decades many reports have revealed that oxygen vacancies can modulate the coordination,[2] electron states,[3] electrical conductivity,[4] surface structure,[5] and acid-base property over catalysts.[6,7] In the presence of oxygen vacancies, the optimization and further activation of adsorbed reactant molecules is helpful for promoting catalytic performance. For example, oxygen vacancies are important sites facilitating the adsorption of fatty acid to form aldehyde over reducible oxides such as TiO_2, ZrO_2, Fe_2O_3, and CeO_2.[8-11] Liu *et al.*demonstrated that oxygen vacancies promote the electrical conductivity of TiO_x and offer strong metal–support interaction to enable the smaller metal particles size, achieving higher catalytic

1

activity, and higher stability of supported metal nanoparticles.[12] Oxygen vacancies and surface lattice hydroxyl constituting frustrated Lewis pair can accelerate CO_2 photocatalytic reduction over oxyhydroxide.[13] To date, considerable research has focused on the role of oxygen vacancies over metal oxides in catalysis.[14] However, the investigation of oxygen vacancies in nonmetal oxides remains rare due to the difficulty in reducing nonmetal oxides and the limitation of the variety of nonmetal oxides. Therefore, how oxygen vacancies affect catalytic reaction over nonmetal oxides seems interesting and desirable.

Propene is one of the most useful building blocks in industry.[15-17] Oxidative dehydrogenation of propane (ODHP) is a preferable choice available to produce propene because of the advantages of coking-free and no equilibrium limit.[18,19] However, due to the poor propene selectivity the commercial implementation of propene in ODHP is still not impressive even after decades of research.[15] Substantial efforts have been made on the modification of acid–base properties of catalysts to facilitate the desorption of propene from the catalyst surface in ODHP, and thus to improve the selectivity to propene. By using alkali additives (e.g., Li, K, Rb cations) to increase the basicity of some catalysts such as V_2O_5/TiO_2, MoO_3/TiO_2,[20,21] MoO_3/MgO–γ-Al_2O_3[22] and V_2O_5/Al_2O_3[23], the selectivity to propene increased with the better propene desorption.[20,21] Some transition metals (e.g., Bi, Mo) have also been used as additives to modify the acid–base properties of the vanadia–alumina based catalysts and enhance the activity of the ODHP.[24] However, whatever additives are used, both the selectivity to propene and the conversion of propane could not be improved at the same time. From these works, the key to improving both of them lies on rapid propene desorption and higher propane adsorption capacity. Considering the role of oxygen vacancy in modulating acid–base property, a rational strategy is expected to construct active catalysts with oxygen vacancies for the ODHP.

Recently, Bao's group has proposed a concept of confined catalysis under cover describing catalytic reaction occurring in a confined space (e.g., the interface between substrate surface and neighboring 2D layer cover).[25] The confined space can optimize adsorption–desorption property owing to its electron modulating ability. Hexagonal boron nitride (BN) was often used as a cover layer to form confined space to adjust electron structure of substrate and thus facilitated catalytic reaction.[26-28] Moreover, very recently, BN acts as good catalyst for ODHP with high propene selectivity and negligible CO_2 emission compared with vanadia-based catalysts.[18,29-31] In this work, we create oxygen vacancies on the surface of BPO_4 hollow spheres covered by few-layer BN with a sandwich-like structure (BN@BPO_4@BN) through high-temperature reduction method. The formation of BN@BPO_4@BN sandwich-like hollow spheres generates a confined space between BPO_4 and BN. Oxygen vacancies were verified by X-ray photoelectron spectroscopy (XPS) and Electron Paramagnetic Resonance (EPR) analysis and its density (ca. 1.02×10^{-5} mol/m^2) was evaluated by NH_3–TPD and BET. The increased activity and selectivity of the ODHP to propene were obtained for BN@BPO_4@BN compared with pure BN because of the synergetic effect between oxygen vacancies and BN. Oxygen vacancies increase the adsorption amount of propane and the confined space weakens the adsorption of propene. Furthermore, the reaction kinetic model undergoes a transformation from Eley–Rideal mechanism into Langmuir–Hinshelwood mechanism in the oxygen vacancies-rich confined space. This investigation enhances our understanding of the role of oxygen vacancy over nonmetal oxide.

Experimental section

Preparation of BPO_4 spheres

Boron oxide (B_2O_3) and diammonium hydrogen phosphate ((NH_4)$_2HPO_4$) were mixed with a 2: 1 molar ratio and grinded in an agate mortar. The mixture was heated at 800 °C for 2 h under ambient atmosphere. After cooling down to room temperature, the product was obtained by grinding and washing using diluted HCl and ultrapure water.

Preparation of BN@BPO_4@BN sandwich-like hollow spheres

The as-obtained BPO_4 spheres were put into a tube furnace and annealed at 900 °C for 0.5 h under NH_3 atmosphere. A series of samples were prepared by prolonging anneal time to adjust the BN mass content. Before annealing, the system was purged for 2 h with NH_3 to ensure the removal of oxygen from the furnace.

Characterization section

XRD data were obtained on an X-ray diffractometer (Bruker D8 Advance). ATR–FTIR was performed on a Nicolet IS 50 apparatus. N_2 adsorption–desorption isotherm measurements were investigated at 77 K on a Micromeritics 3 Flex 3500 instrument. SEM (Hitachi New Generation SU8100) and TEM (TECNAI F30) were employed to study the microstructures of samples. XPS were collected using an X-ray photoelectron spectrometer (Thermo Scientific Escalab 250). TG was carried out in flowing air atmosphere (20 mL/min) with a thermoanalyzer (Netzsch STA 449F3) in alumina crucibles. EPR was conducted on a apparatus (Bruker-A 300) at room temperature.

Catalytic activity test

The selective oxidative dehydrogenation reaction was performed at atmospheric pressure in a fixed-bed reactor. The catalyst (50 mg) mixed with quartz sand (200 mg, 60–80 mesh) was put into a U-type quartz tube (4 mm inner diameter and 6 mm external diameter) between two quartz wools. Then the tube was placed in a vertical furnace and heated up to the target reaction temperature. The feed gas consisting of nitrogen, oxygen, and propane was controlled by a mass flow meter (Sevenstar). The product components were analyzed on an on-line gas chromatograph (Pannatek A90) equipped with a flame ionization detector (FID) and a Nickel reformer.

Temperature-programmed desorption (TPD) test

The test was conducted on an on-line gas chromatograph (Pannatek A90) equipped with a FID. Before the test, the powder sample (20 mg) was pre-treated at 300 ºC in N_2 (20 mL/min) for 1 h in a U-type quartz tube (4 mm inner diameter and 6 mm external diameter) between two quartz wools. Then the pre-treated sample was cooled down to room temperature and saturated with propane or propene (10 mL/min) for 30 min. Subsequently, the system was flushed with N_2 flow (20 mL/min) for 1 h to ensure the removal of physically adsorbed propane or propene. Desorption of probe gas was performed over the temperature range from room temperature to 800 °C at a ramping rate of 10 °C/min. The acid amount of samples was carried out by NH_3 temperature-programmed desorption–mass spectrometry (NH_3 TPD–MS) on an AutoChem II 2920 apparatus.

Results and discussion

Characterization of samples

The BN@BPO_4@BN samples were prepared by high-temperature reduction of BPO_4 spheres under NH_3 atmosphere. The X-ray diffraction (XRD) patterns of various samples were collected (Figure S1a). The peaks at 24.5, 40.0, 48.8, and 63.7º are ascribed to BPO_4 crystal (JCPDS 06-0297). No characteristic peak corresponding to BN in BN@BPO_4@BN occurs due to its low content and high dispersion. Further information about the components was obtained by attenuated total internal reflectance Fourier transform infrared spectroscopy (ATR–FTIR) (Figure S1b). The peaks at 1059, 909, 607, and 544 cm⁻¹ originate from BPO_4.[32] As expected, two absorption bands at 1369 and 818 cm⁻¹ belonging to the characteristic vibration of BN are observed in BN@BPO_4@BN, revealing the formation of BN.

Field emission scanning electron microscope (SEM) and field emission transmission electron microscope (TEM) were employed to study the microstructures of samples (Figure 1). It can be seen that BPO_4 spheres with hollow structure were obtained successfully (Figure 1a and 1c). HRTEM image (Figure 1d) from the surface of BPO_4 spheres presents that BPO_4 spheres are covered by a B–P–O amorphous layer.[19] After annealing the BPO_4 spheres under NH_3 atmosphere at 900 ºC, its overall structure has no obvious change (Figure 1b and 1e–f). In the HRTEM images (Figure 1g–h), there are clear crystal lattices of 0.36 and 0.34 nm corresponding to the (101) plane of BPO_4 and the (002) plane of BN,[33] respectively. Obviously, the BPO_4 sphere is covered by few-layer BN with a thickness of 1.5–3 nm. It is worth noting that the B–P–O amorphous layer on the BPO_4 spheres surface disappeared, which is due to the in-situ transformation of the B–P–O amorphous layer to BN layer under NH_3 gas atmosphere at high temperature.[34] For more detailed information about the inside surface of hollow spheres, a notched sphere was selected and, impressively, exhibited hollow

structure with a coverage of BN on both surfaces of the BPO_4 sphere (Figure S2), demonstrating the sandwich-like hollow sphere structure of $BN@BPO_4@BN$. The confined space is thus formed at the interface between BN layer and BPO_4 sphere.[35] In addition, the surface area of BPO_4 spheres and $BN@BPO_4@BN$ were measured to be 3.6 and 5.7 m^2/g, respectively (Table S1). The incremental surface area after annealing further confirms the formation of the sandwich-like hollow sphere structure.

To further shed light on the surface chemical composition of BPO_4 spheres and $BN@BPO_4@BN$, XPS analysis was performed. There are P, B, O, N elements in both BPO_4 spheres and $BN@BPO_4@BN$ (Figure S3a,b). In the N 1s core-level spectrum (Figure 2a), as expected, the main peak at 398.1 eV attributed to N–B bond was detected in $BN@BPO_4@BN$,[33,36] indicating the formation of BN. B–N bond can also be found at 190.6 eV in the B 1s core-level spectrum (Figure S3c). The P 2p core-level spectrum of BPO_4 spheres (Figure 2b) is composed of a spin–orbit doublet with peaks at 135.2 and 134.3 eV, associated with P^{5+} cations.[37] The broader full-width at half-maximum of the P 2p core-level spectrum for $BN@BPO_4@BN$ can be decomposed into P^{5+} and P^{4+} components. It is obvious that P^{4+} cations come from BPO_4 surface, which could be caused by the introduction of oxygen vacancies under NH_3 atmosphere at annealing process.[38]

EPR is a sensitive and effective method to detect oxygen vacancies. For $BN@BPO_4@BN$ (Figure 2c), the signal at $g = 2.0027$ is assigned to the oxygen vacancy of BPO_4.[39,40] This result is a compelling evidence for the formation of oxygen vacancies on the surface of BPO_4.

In order to measure BN mass content in $BN@BPO_4@BN$, thermogravimetric analysis (TG) was carried out in air flow. According to the oxidation equation of BN (), we can obtain the increment at the end of oxidation process (Figure 2d). Therefore, the mass fraction of BN in $BN@BPO_4@BN$ was measured to be 5.5 wt%.

Catalytic activity and kinetics

The various samples were used to catalyze selective oxidation of propane to propene. $BN@BPO_4@BN$ shows 13.6% propane conversion far more than that of BPO_4 spheres (1.6%) and blank comparison (0.9%) (Table 1). While for commercial BN with the same BN mass (2.75 mg) contained in $BN@BPO_4@BN$ used for the reaction, $BN@BPO_4@BN$ has a better propane conversion than commercial BN with the almost same selectivity. From Table 1, it is evident that BN is the source of catalytic activity for ODHP. When increasing commercial BN mass (5 mg) to obtain the similar conversion as $BN@BPO_4@BN$, the propene selectivity falls from 75.3% to 73.0%. As a whole, $BN@ BPO_4@BN$ with the same BN content gains an advantage over commercial BN, embodied in the higher propene selectivity at the same propane conversion level.

The apparent activation energy of $BN@BPO_4@BN$ and commercial BN was measured at below 10% propane conversion. $BN@BPO_4@BN$ has a lower apparent activation energy (186 kJ/mol) than that of commercial BN (239 kJ/mol) (Figure 3a). The obvious decrease of activation energy reveals the change of reaction mechanism and the key role of oxygen vacancies.[41] According to Hermans' report, Eley–Rideal mechanism is applicative in the ODHP for BN catalyst and there is a tendency to reach a platform of C_3H_8 consumption rate limit with the increase of O_2 partial pressure.[18] However, obviously, the trend of the reaction rate goes up and then down (Figure 3b). Therefore, the reaction follows Langmuir–Hinshelwood mechanism over $BN@BPO_4@BN$ catalyst (Scheme 1), that is, the dissociative C_3H_8 is adsorbed and reacts with O_2 on the catalyst surface. The adsorbed C_3H_8 could originate from the positive effect of BPO_4 support with oxygen vacancies.

To gain more insight into the effect of BN mass content on the catalytic activity, the $BN@BPO_4@BN$ samples with different annealing time (1, 3 and 5 h) were prepared to vary the BN mass content. On increasing annealing time, no obvious change in the micromorphology was observed for the samples, but the thickness of the BN shell increases (Figure S4 and S5). The increased thickness of BN improves the BN mass content of the $BN@BPO_4@BN$ samples (Table S3). Moreover, the propane conversion rises rapidly and then holds stable and even declines with the increase of BN mass content (Figure 3c). By contrast, the activity of commercial BN with the similar mass level of $BN@BPO_4@BN$ keeps growing with increasing BN mass. For the $BN@BPO_4@BN$ samples, the growth of conversion can be ascribed to the increased BN content[18,42], whereas the stunted growth and even downtrend is caused by the decreased interface area between BPO_4 and BN.[43] Furthermore, by plotting propene selectivity against propane conversion (See Figure 3d) the $BN@BPO_4@BN$

4

sample shows higher propene selectivity at a similar conversion level than commercial BN.

The long-term stability of BN@BPO$_4$@BN with 8.5 wt% BN was investigated due to the highest propane conversion (Figure S6). It shows stable catalytic performance occurring at low O$_2$ concentration, revealing the relative stability of oxygen vacancies under this condition. Interestingly, the selectivity to propene declines with the decrease of oxygen concentration at the beginning of the reaction, which is caused by the catalytic cracking of propane on the catalyst surface,[44] further confirming the transformation of Eley–Rideal mechanism to Langmuir–Hinshelwood mechanism.

The reason of enhanced performance

In view of the role of oxygen vacancy in modulating acid–base property closely related to the catalytic performance, the acid site species of catalysts were investigated by pyridine adsorbed FTIR firstly (Figure 4a). Two adsorption bands at 1587 and 1440 cm^{-1} in BN@BPO$_4$@BN are attributed to typical Lewis acid sites, verifying the existence of oxygen vacancies.[45] The adsorption band at 1540 cm^{-1} in BPO$_4$ spheres can be ascribed to Brønsted acid sites such as surface hydroxyl.[45] Both species of acid sites have adsorption band at 1486 cm^{-1}. The distribution and amount of acid sites were further measured by NH$_3$–TPD (Figure 4b–d). BPO$_4$ spheres and commercial BN have barely acid sites. By contrast, there are two NH$_3$ desorption peaks at ca. 140 and 380 °C for BN@ BPO$_4$@BN corresponding to weak and strong acid sites, respectively. The formation of acid sites in BN@BPO$_4$@BN is due to two possibilities: 1) the introduction of oxygen vacancies on the BPO$_4$ support could be responsible for the acid site, because oxygen vacancy is a typical Lewis acid species;[13,46] 2) other acid species (e.g., hydroxyl) are introduced and bind to NH$_3$. Interestingly, the strong acid sites increased and the weak acid sites decreased after reaction (Figure 4b). The increase of strong acid sites for used BN@ BPO$_4$@BN could be due to the formation of amorphous B(OH)$_x$ O$_{3-x}$ phase.[42] In light of the decrease of both oxygen vacancies and weak acid sites in used BN@BPO$_4$@BN (Figure S7), we attribute the weak acid sites to oxygen vacancies and the strong acid sites to other acid species. Meanwhile, the precise amount of oxygen vacancies was monitored by thermal conductivity detector (TCD) signal and the detected spectrum was deconvoluted by Gaussian fitting (Figure 4c–d). The total amount of acid sites is 1.94×10^{-4} mol/g for BN@BPO$_4$@BN and 1.78×10^{-4} mol/g for used BN@BPO$_4$@BN (Table S2), respectively. Furthermore, the weak acid amount was estimated to be 3.88×10^{-5} mol/g for BN@BPO$_4$@BN (Figure 4d). Therefore, the concentration of oxygen vacancies on the BPO$_4$ surface was evaluated to be ca. 1.02×10^{-5} mol/m^2 that is equivalent to the concentration of Lewis acid sites by combining acid amount and surface area (Table S1).

The effect of oxygen vacancies on catalytic performance was confirmed by the propane conversion change *vs* stream on time (Figure S7a). The propane conversion decreases with the reduction of oxygen vacancies on the surface of BN@BPO$_4$@BN. Meanwhile, the propene selectivity has no obvious change, showing that the selectivity of propene is not related to the amount of oxygen vacancies.

The seemingly trivial reactant adsorption and product desorption on the catalyst surface are, in fact, the fundamental steps in heterogeneous catalytic reaction. First, absorption is accountable for the pre-activation of reactants,[47] and appropriate adsorption strength ensures the movement of reactants on the catalyst surface. On the other hand, the products should be quickly separated from the catalyst surface to avoid back and/or side reactions and to accelerate the recycling of active sites.[48] Hence, the adsorption of the reactant propane (C$_3$H$_8$) and the desorption of the product propene (C$_3$H$_6$) on the catalyst surface are highly concerned in the reaction. The adsorption/desorption performance can be tested by temperature-programmed desorption (TPD) (See Figure 5). The similar shape and location of the propane desorption peak were observed at ca. 472 °C for the BN-contained samples (See Figure 5a), indicating that the chemisorption peak originates from BN. Interestingly, a larger desorption peak appears at lower temperature region for BN@BPO$_4$@BN compared with that of BN and BPO$_4$ spheres, meaning that BN@BPO$_4$@BN has a better adsorption of propane than BN and BPO$_4$. Since surface oxygen vacancies can serve as adsorption sites,[49-51] the increased chemisorption capacity of BN@BPO$_4$@BN is caused by rich oxygen vacancies on BPO$_4$ surface (Figure 2). Moreover, the decreased chemisorption of propane in used BN@BPO$_4$@BN indicates the reduce of oxygen vacancies over used BN@BPO$_4$@BN (See Figure 5a) which is also confirmed by XPS analysis (Figure S7).

5

Therefore, the oxygen vacancies-rich BPO_4 also act as important reaction sites. In addition, the adsorption of propane by oxygen vacancies demonstrates that C_3H_8 is able to enter the confined space between BN and BPO_4. Moreover, C_3H_6-TPD was also employed to study the chemisorption performance of propene. BN@BPO_4@BN has a desorption temperature lower than that of BN and BPO_4 spheres, but similar to that of used BN@BPO_4@BN (Figure 5b). This indicates that BN@BPO_4@BN has better propene desorption performance than BN and BPO_4, which could be due to the effect of the confined space between BN and BPO_4.[52,53] Therefore, the confined space is favorable for the desorption of propene in the reaction. Taken together, the enhanced chemisorption of propane and the weakened chemisorption of propene, corresponding to the adsorption/desorption process of reactants/products in heterogeneous catalysis, makes a contribution to the higher conversion and selectivity for BN@BPO_4@BN. Besides, the synergetic effect between oxygen vacancies-rich BPO_4 and the confined space boosts the oxidative dehydrogenation of propane to propene.

Proposed reaction mechanism

Based on the above results and discussion, a schematic of ODHP to propene over BN@BPO_4@BN is given in Figure 6. Because of the better adsorption of propane by oxygen vacancies, most propane enters into the confined space at the interface of the BN shell and the BPO_4 core through pores. In the confined space, propane molecules are bound to the oxygen vacancies on the BPO_4 surface and oxygen molecules are adsorbed on the BN surface. Due to the confinement of the surfaces of BPO_4 and BN, the reaction of molecular oxygen and propane can be viewed as on the same quasi-planar surface. Then, activated oxygen molecules react with adsorbed propane molecules instead of dissociative propane, and thus the reaction kinetic model undergoes a transformation from Eley–Rideal mechanism on the surface of pure BN [18] to Langmuir–Hinshelwood mechanism for BN@BPO_4@BN. The generated propene molecules rapidly escape due to the weakened adsorption intensity resulted from the confined space effect.[52,53] Therefore, a synergetic effect of oxygen vacancies and confined space occurs for ODHP.

Conclusions

In summary, we present a detailed study on oxygen vacancies in nonmetal oxide through rational catalyst design. Oxygen vacancies were constructed on the BPO_4 surface under the BN cover with a sandwich-like hollow sphere structure. The density of oxygen vacancies was estimated to be ca. 1.02×10^{-5} mol/m^2. The as-obtained catalyst BN@BPO_4@BN achieved better activity and selectivity in ODHP than commercial BN catalyst. Oxygen vacancies and the confined space result in the transformation of the reaction kinetic model of ODHP from Eley–Rideal mechanism (for BN only) to Langmuir–Hinshelwood mechanism, leading to a lower activation energy of BN@BPO_4@BN (186 kJ/mol) than that of commercial BN (239 kJ/mol). Moreover, experimental results indicate that oxygen vacancies-rich BPO_4 increases the adsorption amount of propane and the confined space makes easier desorption of propene, which is helpful for the recycle of active sites. Therefore, oxygen vacancies act as important reaction sites and there exists a synergetic effect between oxygen vacancies-rich BPO_4 and BN for ODHP. This work the application of nonmetal oxides with oxygen vacancies in the field of catalysis.

A cknowledgements

Literature Cited

1. Li H, Li J, Ai Z, Jia F, Zhang L. Oxygen Vacancy-Mediated Photocatalysis of BiOCl: Reactivity, Selectivity, and Perspectives. *Angewandte Chemie International Edition.* 2018;57(1):122-138.

2. Wu Q, Zheng Q, van de Krol R. Creating Oxygen Vacancies as a Novel Strategy To Form Tetrahedrally Coordinated Ti4+ in Fe/TiO2 Nanoparticles. *The Journal of Physical Chemistry C.* 2012;116(12):7219-7226.

3. Sun Y, Gao S, Lei F, Xie Y. Atomically-thin two-dimensional sheets for understanding active sites in catalysis. *Chemical Society Reviews.* 2015;44(3):623-636.

4. Wang Z, Mao X, Chen P, et al. Understanding the Roles of Oxygen Vacancies in Hematite-Based Photoelectrochemical Processes.*Angewandte Chemie International Edition.* 2019;131(4):1042-1046.

5. Liu D, Wang C, Yu Y, et al. Understanding the Nature of Ammonia Treatment to Synthesize Oxygen Vacancy-Enriched Transition Metal Oxides. *Chem.* 2019;5(2):376-389.

6. Abee MW, Cox DF. NH3 chemisorption on stoichiometric and oxygen-deficient SnO2(110) surfaces. *Surface Science.*2002;520(1):65-77.

7. Liu B, Li C, Zhang G, Yan L, Li Z. Direct synthesis of dimethyl carbonate from CO2 and methanol over CaO–CeO2 catalysts: the role of acid–base properties and surface oxygen vacancies. *New Journal of Chemistry.* 2017;41(20):12231-12240.

8. Hengsawad T, Jindarat T, Resasco DE, Jongpatiwut S. Synergistic effect of oxygen vacancies and highly dispersed Pd nanoparticles over Pd-loaded TiO_2 prepared by a single-step sol–gel process for deoxygenation of triglycerides.*Applied Catalysis A: General.* 2018;566:74-86.

9. Peng B, Zhao C, Kasakov S, Foraita S, Lercher JA. Manipulating Catalytic Pathways: Deoxygenation of Palmitic Acid on Multifunctional Catalysts. *Chemistry – A European Journal.*2013;19(15):4732-4741.

10. Pan X, Yang M-Q, Fu X, Zhang N, Xu Y-J. Defective TiO_2 with oxygen vacancies: synthesis, properties and photocatalytic applications. *Nanoscale.* 2013;5(9):3601-3614.

11. Pestman R, Koster RM, Pieterse JAZ, Ponec V. Reactions of Carboxylic Acids on Oxides: 1. Selective Hydrogenation of Acetic Acid to Acetaldehyde. *Journal of Catalysis.* 1997;168(2):255-264.

12. Liu G, Li J, Fu J, et al. An Oxygen-Vacancy-Rich Semiconductor-Supported Bifunctional Catalyst for Efficient and Stable Zinc–Air Batteries. *Advanced Materials.*2019;31(6):1806761-1806767.

13. Wang X, Lu L, Wang B, et al. Frustrated Lewis Pairs Accelerating CO_2 Reduction on Oxyhydroxide Photocatalysts with Surface Lattice Hydroxyls as a Solid-State Proton Donor. *Advanced Functional Materials.*2018;28(43):1804191-1804199.

14. Wang G, Yang Y, Han D, Li Y. Oxygen defective metal oxides for energy conversion and storage. *Nano Today.* 2017;13:23-39.

15. Cavani F, Ballarini N, Cericola A. Oxidative dehydrogenation of ethane and propane: How far from commercial implementation? *Catalysis Today.* 2007;127(1-4):113-131.

16. Chen K, Bell AT, Iglesia E. Kinetics and mechanism of oxidative dehydrogenation of propane on vanadium, molybdenum, and tungsten oxides. *The Journal of Physical Chemistry B.*2000;104(6):1292-1299.

17. Wu Z, Kim H-S, Stair PC, Rugmini S, Jackson SD. On the Structure of Vanadium Oxide Supported on Aluminas: UV and Visible Raman Spectroscopy, UV-Visible Diffuse Reflectance Spectroscopy, and Temperature-Programmed Reduction Studies. *The Journal of Physical Chemistry B.* 2005;109(7):2793-2800.

18. Grant JT, Carrero CA, Goeltl F, et al. Selective oxidative dehydrogenation of propane to propene using boron nitride catalysts.*Science.* 2016;354(6319):1570-1573.

19. Liu Q, Wu Y, Xing F, Liu Q, Guo X, Huang C. B2O3@BPO4 sandwich-like hollow spheres as metal-free supported liquid-phase catalysts. *Journal of Catalysis.* 2020;381:599-607.

20. Grzybowska B, Mekšs P, Grabowski R, Wcisto K, Barbaux Y, Gengembre L. Effect of Potassium Addition to V_2O_5/TiO_2 and MoO_3/TiO_2 Catalysts on Their Physicochemical and Catalytic Properties in Oxidative Dehydrogenation of Propane. In: Corberán VC, Bellón SV, eds. *Studies in Surface Science and Catalysis.* Vol 82: Elsevier; 1994:151-158.

21. Grabowski R, Grzybowska B, Samson K, Słoczyński J, Stoch J, Wcisło K. Effect of alkaline promoters on catalytic activity of V_2O_5/TiO_2 and MoO_3/TiO_2 catalysts in oxidative dehydrogenation of propane and in isopropanol decomposition. *Applied Catalysis A: General.* 1995;125(1):129-144.

22. Abello MC, Gomez MF, Cadus LE. Selective oxidation of propane on $MgO/\gamma\text{-}Al_2O_3$-supported molybdenum catalyst: influence of promoters. *Catalysis Letters.* 1998;53(3):185-192.

23. Blasco T, Nieto JML. Oxidative dyhydrogenation of short chain alkanes on supported vanadium oxide catalysts. *Applied Catalysis A: General.* 1997;157(1):117-142.

24. López Nieto JM, Coenraads R, Dejoz A, Vazquez MI. The role of metal oxides as promoters of $V_2O_5/\gamma\text{-}Al_2O_3$ catalysts in the oxidative dehydrogenation of propane. In: Grasselli RK, Oyama ST, Gaffney AM, Lyons JE, eds. *Studies in Surface Science and Catalysis.* Vol 110: Elsevier; 1997:443-452.

25. Fu Q, Bao X. Surface chemistry and catalysis confined under two-dimensional materials. *Chemical Society Reviews.* 2017;46(7):1842-1874.

26. Gao L, Wang Y, Li H, et al. A nickel nanocatalyst within a h-BN shell for enhanced hydrogen oxidation reactions. *Chemical science.* 2017;8(8):5728-5734.

27. Chen S, Li Y, Zhang Z, Fu Q, Bao X. The synergetic effect of h-BN shells and subsurface B in CoB x@ h-BN nanocatalysts for enhanced oxygen evolution reactions. *Journal of Materials Chemistry A.* 2018;6(23):10644-10648.

28. Sun M, Fu Q, Gao L, et al. Catalysis under shell: Improved CO oxidation reaction confined in Pt@ h-BN core–shell nanoreactors. *Nano Research.* 2017;10(4):1403-1412.

29. Lei S, Wang D, Wei S, Dan S, Zhang WP, Lu AH. Edge-hydroxylated Boron Nitride for Oxidative Dehydrogenation of Propane to Propylene. *Chemcatchem.* 2017;9(10):1718-1718.

30. Chaturbedy P, Ahamed M, Eswaramoorthy M. Oxidative Dehydrogenation of Propane over a High Surface Area Boron Nitride Catalyst: Exceptional Selectivity for Olefins at High Conversion. *ACS Omega.* 2018;3(1):369-374.

31. Tian J, Lin J, Xu M, Wan S, Lin J, Wang Y. Hexagonal boron nitride catalyst in a fixed-bed reactor for exothermic propane oxidation dehydrogenation. *Chemical Engineering Science.* 2018;186:142-151.

32. Doğan M, Bayramlı E. The flame retardant effect of aluminum phosphinate in combination with zinc borate, borophosphate, and nanoclay in polyamide-6. *Fire and Materials.* 2014;38(1):92-99.

33. Liu Q, Chen C, Du M, et al. Porous Hexagonal Boron Nitride Sheets: Effect of Hydroxyl and Secondary Amino Groups on Photocatalytic Hydrogen Evolution. *ACS Applied Nano Materials.* 2018;1(9):4566-4575.

34. Bamberger CE, Begun GM. Synthesis of BN Using BPO4 as the Boron Source. *Journal of the American Ceramic Society.* 1986;69(5):C-95-C-97.

35. Deng D, Novoselov KS, Fu Q, Zheng N, Tian Z, Bao X. Catalysis with two-dimensional materials and their heterostructures. *Nature Nanotechnology.* 2016;11:218.

36. Liu Q, Xu Y, Qiu X, Huang C, Liu M. Chemoselective hydrogenation of nitrobenzenes activated with tuned Au/h-BN. *Journal of Catalysis.* 2019;370:55-60.

37. Chowdari B, Rao GS, Leo C. XPS studies and defect structure of pure and Li-doped SrBPO51. *Materials research bulletin.* 2001;36(3-4):727-736.

38. Liu Q, Wu Y, Zhang J, et al. Plasmonic MoO3-x nanosheets with tunable oxygen vacancies as efficient visible light responsive photocatalyst. *Applied Surface Science.* 2019;490:395-402.

39. Kaftelen H, Ocakoglu K, Thomann R, Tu S, Weber S, Erdem E. EPR and photoluminescence spectroscopy studies on the defect structure of ZnO nanocrystals. *Physical Review B.* 2012;in press(1):6335-6335.

40. Fujita T, Ishida T, Shibamoto K, et al. CO Oxidation over Au/ZnO: Unprecedented Change of the Reaction Mechanism at Low Temperature Caused by a Different O2 Activation Process. *ACS Catalysis.* 2019:8364-8372.

41. Yang J, Hu S, Fang Y, et al. Oxygen Vacancy Promoted O2 Activation over Perovskite Oxide for Low-Temperature CO Oxidation.*ACS Catalysis.* 2019;9(11):9751-9763.

42. Love AM, Thomas B, Specht SE, et al. Probing the Transformation of Boron Nitride Catalysts under Oxidative Dehydrogenation Conditions. *Journal of the American Chemical Society.* 2018;141(1):182-190.

43. Chen G, Zhao Y, Fu G, et al. Interfacial Effects in Iron-Nickel Hydroxide–Platinum Nanoparticles Enhance Catalytic Oxidation. *Science.* 2014;344(6183):495-499.

44. Grabowski R. Kinetics of Oxidative Dehydrogenation of C2-C3 Alkanes on Oxide Catalysts. *Catalysis Reviews-science and Engineering - CATAL REV-SCI ENG.* 2006;48:199-268.

45. Wang Y, Chen L, Cao H, et al. Role of oxygen vacancies and Mn sites in hierarchical Mn_2O_3/$LaMnO_{3-\delta}$perovskite composites for aqueous organic pollutants decontamination.*Applied Catalysis B: Environmental.* 2019;245:546-554.

46. Wang Y, Wang F, Song Q, Xin Q, Xu S, Xu J. Heterogeneous Ceria Catalyst with Water-Tolerant Lewis Acidic Sites for One-Pot Synthesis of 1,3-Diols via Prins Condensation and Hydrolysis Reactions.*Journal of the American Chemical Society.* 2013;135(4):1506-1515.

47. Corma A, Ortega FJ. Influence of adsorption parameters on catalytic cracking and catalyst decay. *Journal of Catalysis.*2005;233(2):257-265.

48. Marszewski M, Cao S, Yu J, Jaroniec M. Semiconductor-based photocatalytic CO 2 conversion. *Materials Horizons.*2015;2(3):261-278.

49. Shukri G, Diño WA, Dipojono HK, Agusta MK, Kasai H. Enhanced molecular adsorption of ethylene on reduced anatase TiO_2 (001): role of surface O-vacancies. *RSC Advances.* 2016;6(95):92241-92251.

50. Kämper A, Hahndorf I, Baerns M. A molecular mechanics study of the adsorption of ethane and propane on V_2O_5 (001) surfaces with oxygen vacancies. *Topics in Catalysis.* 2000;11(1):77-84.

51. Saputera WH, Tahini HA, Sabsabi M, et al. Light-Induced Synergistic Multidefect Sites on TiO_2/SiO_2 Composites for Catalytic Dehydrogenation. *ACS Catalysis.* 2019;9(3):2674-2684.

52. Sun Y, Li X, Wang J, et al. Carbon film encapsulated Pt NPs for selective oxidation of alcohols in acidic aqueous solution.*Applied Catalysis B: Environmental.* 2017;218:538-544.

53. Wang T, Gao L, Hou J, et al. Rational approach to guest confinement inside MOF cavities for low-temperature catalysis.*Nature Communications.* 2019;10(1):1340.
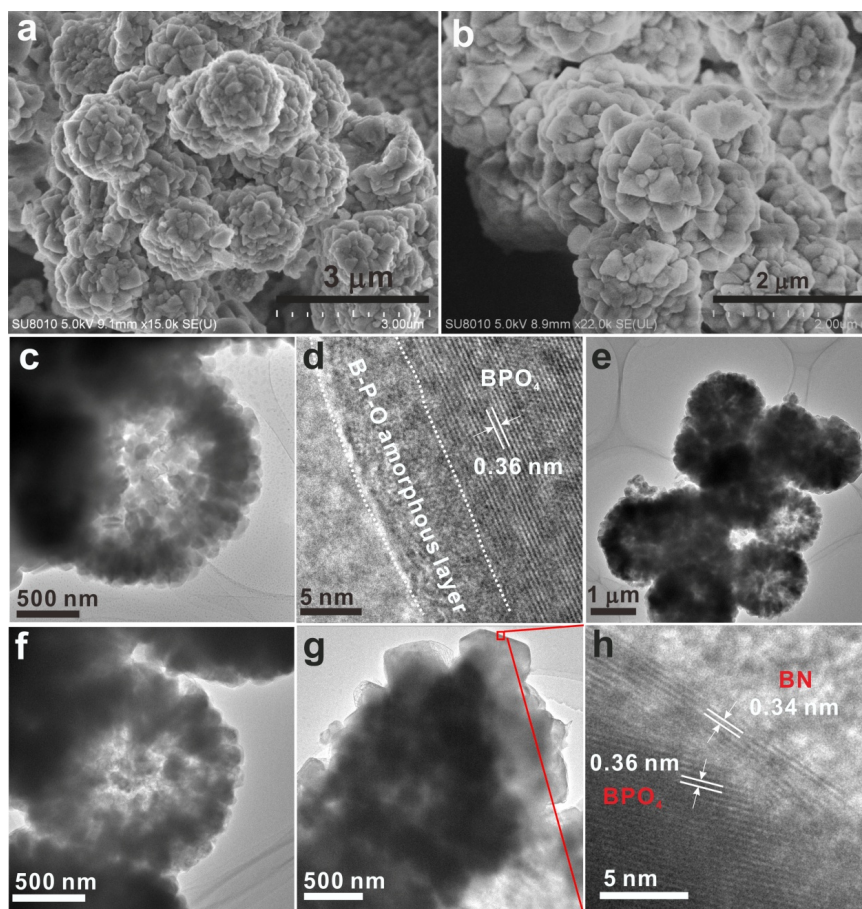
Figures and tables

Figure 1. Morphology of samples. SEM images of (**a**) BPO_4 spheres and (**b**) BN@BPO_4@BN, respectively. TEM and HRTEM images of (**c** –**d**) BPO_4 spheres and (**e** –**h**) BN@BPO_4@BN sandwich-like hollow spheres.

Hosted file

`image3.emf` available at https://authorea.com/users/325457/articles/453437-nonmetal-oxygen-vacancies-for-catalysis-under-cover

Figure 2. Component of BN@BPO_4@BN. (**a**) core-level N 1s and (**b**) core-level P 2p of XPS spectra for BPO_4 spheres and BN@BPO_4@BN. (**c**) EPR spectrum of oxygen vacancies in BN@BPO_4@BN. (**d**) TG curve of BN@BPO_4@BN in air flow.

Table 1. Catalytic performance of various catalysts for oxidative dehydrogenation of propane to propene.

Sample	Propane Cov. (%)	Propene Sel. (%)
BN@BPO_4@BN (50 mg)	13.6	75.2
Commercial BN (2.75 mg)	9.3	75.3
Commercial BN (5 mg)	13.9	73.0
BPO_4 spheres (50 mg)	1.6	82.1
No catalyst	0.9	75.0

Reaction conditions: 15 kPa O_2, 30 kPa C_3H_8, N_2 balance, 20 mL/min, 550 °C. 50 mg BN@BPO$_4$@BN contains ca. 2.75 mg BN.

Scheme 1. Different reaction models on the catalyst surface.

Hosted file

`image4.emf` available at https://authorea.com/users/325457/articles/453437-nonmetal-oxygen-vacancies-for-catalysis-under-cover

Figure 3. Reaction kinetics. (**a**) The apparent activation energy of BN@BPO$_4$@BN and commercial BN for ODHP. (**b**) Rate of C_3H_8consumption as a function of O_2 partial pressure (C_3H_8 partial pressure constant at 0.2 atm). (**c**) Catalytic performance of various BN@BPO$_4$@BN samples and commercial BN for ODHP. (**d**) Selectivity to propene plotted against propane conversion for ODHP.

Hosted file

`image5.emf` available at https://authorea.com/users/325457/articles/453437-nonmetal-oxygen-vacancies-for-catalysis-under-cover

Figure 4. Acid species characterization. (**a**) Pyridine adsorbed FTIR for BN@BPO$_4$@BN and BPO$_4$. NH$_3$–TPD of different catalysts monitored by (**b**) mass spectrometry (MS) and (**c**) TCD. (**d**) Deconvolution of NH$_3$ desorption peak for BN@BPO$_4$@BN.

Hosted file

`image6.emf` available at https://authorea.com/users/325457/articles/453437-nonmetal-oxygen-vacancies-for-catalysis-under-cover

Figure 5. Adsorption performance. (**a**) C_3H_8-TPD and (**b**) C_3H_6-TPD profiles for different samples.
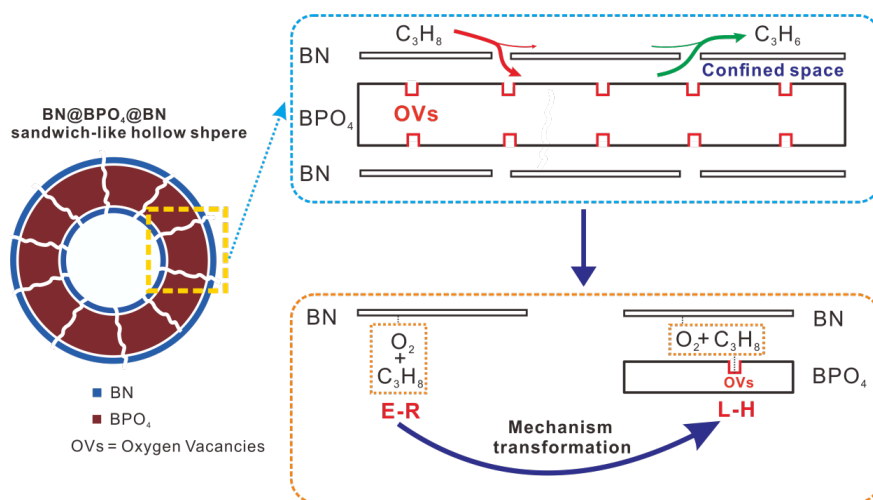

Figure 6. Schematic of proposed reaction mechanism. E–R: Eley–Rideal mechanism. L–H: Langmuir–Hinshelwood mechanism.

11